

See discussions, stats, and author profiles for this publication at: <https://www.researchgate.net/publication/374913464>

Understanding AP/HTPB composite propellant combustion from new perspectives

Article in Combustion and Flame · October 2023

DOI: 10.1016/j.combustflame.2023.113108

CITATIONS

7

READS

123

2 authors:



Yu Cang
Peking University

4 PUBLICATIONS 15 CITATIONS

[SEE PROFILE](#)



Lipo Wang
Shanghai Jiao Tong University

102 PUBLICATIONS 1,035 CITATIONS

[SEE PROFILE](#)

Understanding AP/HTPB composite propellant combustion from new perspectives

Yu Cang^a, Lipo Wang^{a,*}

^aUM-SJTU Joint Institute, Shanghai Jiao Tong University, 800th Dongchuan Road, Minhang District, 200240, Shanghai, China

Abstract

Combustion of the AP/HTPB composite propellant at the mesoscale is simulated by a partitioned numerical framework, in which the unsteady solid-phase conduction, gas-solid interface regression, and gaseous combustion are sequentially calculated on two sets of overlapped grids. The gas-solid interface is traced by the level-set method. The mass and species exchange conditions at the gas-solid interface are converted into source terms by the immersed-boundary method. Effectiveness of the entire framework is justified by applying the integrated solver to a Miller pack example. The predicted burning rates show good agreement with experimental data over a wide range of pressure conditions, and the gas-phase temperature field clearly depicts the final diffusion flame. The flame zone closely above the regressing interface can be identified by the fluctuation of the projected velocity components perpendicular to the main stream direction. Statistical results conditional on Lagrangian tracing of fluid parcels released from the AP and binder parts show distinction between the oxidizer-rich and fuel-rich flames in terms of the reaction intensity and the flame structure.

Novelty and Significance

From the algorithm/simulation perspective: a partitioned numerical solution framework is built upon overlapped structured (for the gas phase) and unstructured (for the solid phase) meshes; the level-set approach is used on the unstructured mesh to identify solid-gas interface with complex geometry. From the analysis perspective: the flame front is newly defined in terms of the tangential velocity components; the fuel/oxidizer evolution pattern is analyzed from conditional statistics based on Lagrangian tracing; new insights in heterogeneous combustion include, for instance, effects of pressure on the tangential velocity fluctuation and flame properties conditional on different ingredients.

Author Contributions

Yu Cang: Coding and calculation, Visualization, Data analyses, Initial writing; **Lipo Wang:** Funding acquisition, Conceptualization, Technical discussion, Finalized writing.

Keywords: Composite propellant combustion, Gas-Solid interface, Flame front, Conditional statistics, Lagrangian tracing

2020 MSC: 76T30, 80A32

1. Introduction

Composite solid propellants are widely used for the purposes of propulsion and power generation. In most cases, solid propellants are typically in the form of composite with complex morphology. A representative example is ammonium perchlorate (AP) crystals embedded in a hydroxyl-terminated polybutadiene (HTPB) binder. The advantages of such composite include safety, high energy density and low cost [1]. Especially, the AP/HTPB composite propellant is favored for its capability to control the burning rate by adjusting the propellant structure, such as the AP particle size, packing density, and distribution [2]. Effective engineering design of the AP/HTPB organization inside the propellant will benefit from reliable predictions, which is, however, quite challenging because of the involved multi-physics and multi-scales. In this sense, more insightful understanding of the AP/HTPB composite propellant combustion process is important and meaningful.

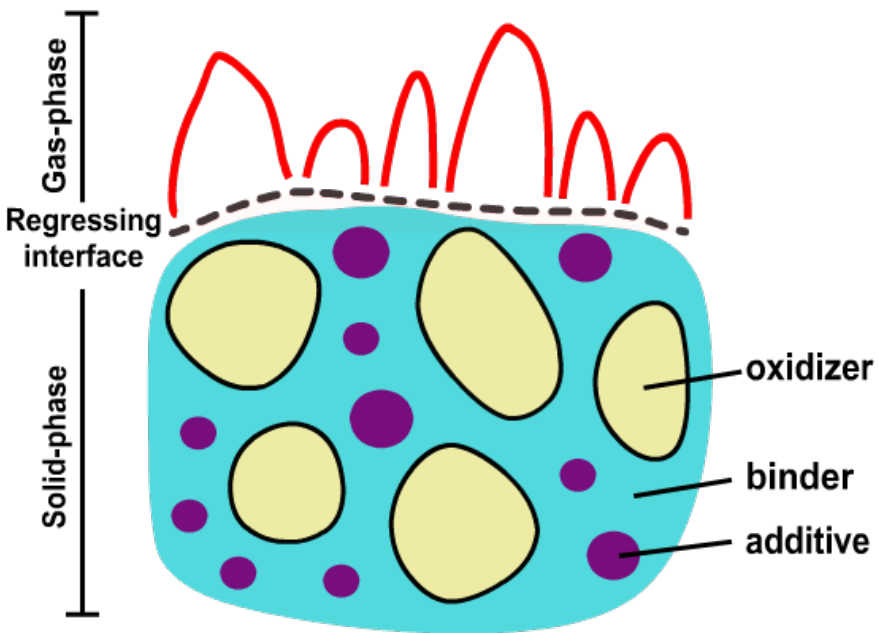


Figure 1: Illustration of the heterogeneous combustion. In the solid phase, typical compositions include the oxidizer crystals (e.g., AP in this study), the binder (e.g., HTPB in this study), and the additives (e.g., aluminum powders, but not considered in this study). Because of the complex solid structure, the regression rate varies locally to generate a corrugated gas-solid interface.

For engineering predictions, the key step is knowledge of the flame structure at the mesoscale level [3], where detailed sub-processes are numerically resolved, including the AP particle resolution, solid phase conduction, gaseous phase combustion and the strong coupling in between. As illustrated in Fig. 1, gaseous combustion takes place above the solid propellant, where ingredient grains are randomly packed. Once ignited, the solid material undergoes

*Corresponding author.

Email addresses: yu.cang@sjtu.edu.cn (Yu Cang), lipo.wang@sjtu.edu.cn (Lipo Wang)

15 complicated evolution (e.g., sublimation, pyrolysis, decomposition and gasification). Variation of the local regression
16 rate leads to a corrugated gas-solid interface.

17 Over the past 30 years, there are continuous advancements in experimental diagnostics of the composite combus-
18 tion. However, direct measurements of some important physical properties are still challenging due to the extremely
19 small scales and demanding operating conditions (e.g., very high pressure and interference from the particles emitted
20 from the composite itself). Alternatively, numerical simulation plays an irreplaceable role. High quality numerical
21 results depend on reasonable combustion models and effective numerical algorithms.

22 Numerous efforts have been made for developing the simulation platforms [4, 5]. The existing skeleton algo-
23 rithms are summarized as follows. Assuming the gas-solid interface to be single-valued, a mapping technique is then
24 introduced to transform the irregular physical domain to regular computational domain partitioned into fine Carte-
25 sian grids, on which the governing equations are discretized by the finite-difference method. If possible, dynamic
26 refinement near the regressing interface is made [6, 7] from the consideration of accuracy and efficiency. Despite
27 the prevailing applications, such a monolithic solution strategy will inevitably necessitate solving large coupled linear
28 systems at each time step. The connecting conditions across the gas-solid interface need to be simplified as well; oth-
29 erwise, the discretization procedure would be rather complicated. Moreover, the oversimplified single valued interface
30 condition may violate real cases with strongly variable local burning rates.

31 Recently, a partitioned numerical framework has been proposed [8, 9] and is applied in this study. After introduc-
32 ing the mesoscale combustion model in Sec. 2, the newly proposed numerical framework is briefly described in Sec. 3,
33 which contains several independent sub-modules and handles the connecting conditions across the gas-solid interface
34 in a distinct manner. Adoption of the level-set method enables identification of generally complicated interfaces. We
35 aim to offer more flexibility in incorporating advanced schemes without loss of accuracy and real physics. Based on
36 the simulation results, the combustion process will be analyzed in Sec. 4 to gain further insights of the propellant
37 morphology effects. This paper is closed with final conclusions in Sec. 5.

38 **2. Problem formulation**

39 Formulation of solid propellant combustion involves physical processes in both the solid phase and the gas phase,
40 the connection in between, and the combustion chemistry, which are elaborated as follows.

41 **2.1. Physical processes**

42 In the gas phase (Ω_g), the three-dimensional continuity, moment, energy and species equations for the low-Mach
43 number reacting flow, together with the ideal gas law for thermodynamic closure, are listed as

$$\frac{\partial \rho_g}{\partial t} + \nabla \cdot (\rho_g \vec{U}) = 0, \quad (1)$$

$$\rho_g \left(\frac{\partial \vec{U}}{\partial t} + \vec{U} \cdot \nabla \vec{U} \right) = -\nabla p + \nabla \cdot \bar{\tau}, \quad (2)$$

$$\rho_g c_p \left(\frac{\partial T_g}{\partial t} + \vec{U} \cdot \nabla T_g \right) = \nabla \cdot (\lambda_g \nabla T_g) + \frac{\partial p}{\partial t} + \dot{\omega}_T, \quad (3)$$

$$\rho_g \left(\frac{\partial Y_k}{\partial t} + \vec{U} \cdot \nabla Y_k \right) = \nabla \cdot \left(\frac{\lambda_g}{c_p} \nabla Y_k \right) + \dot{\omega}_k, \quad (4)$$

$$p \bar{W} = \rho_g R T_g, \quad (5)$$

where $\frac{\partial}{\partial t}$ is the Eulerian time derivative, $\nabla = (\frac{\partial}{\partial x}, \frac{\partial}{\partial y}, \frac{\partial}{\partial z})^T$, ρ_g is the density of the gaseous mixture, $\vec{U} = (u, v, w)^T$ is the fluid velocity vector, p is the hydrodynamic pressure, R is the gas constant, $\bar{\tau}$ is the viscous stress tensor for the Newtonian fluid, T_g represents the gas-phase temperature, c_p and λ_g are the specific heat and thermal conductivity of the gaseous mixture, respectively, $\dot{\omega}_T$ is the heat release rate due to chemical reaction, Y_k is the mass fraction of the k -th gaseous component with the molecular weight MW_k and chemical source $\dot{\omega}_k$, \bar{W} is the molecular weight of the mixture satisfying $\frac{1}{\bar{W}} = \sum_k \frac{Y_k}{\text{MW}_k}$. The unity-Lewis-number condition is assumed in determining the species diffusivity.

In the solid phase (Ω_s), the unsteady heat conduction equation for the solid temperature T_s is:

$$\rho_s c \frac{\partial T_s}{\partial t} = \nabla \cdot (\lambda_s \nabla T_s), \quad (6)$$

where the solid density ρ_s , the heat capacity c and the thermal conductivity λ_s are spatially varied due to the heterogeneity of the composite propellant.

The gas-solid interface (Γ) is tracked by the level-set approach as the zero-contour of the level-set function, whose evolution is governed by

$$\frac{\partial \phi}{\partial t} + \dot{r}_b |\nabla \phi| = 0, \quad (7)$$

where $|\cdot|$ is the Euclidean norm of vector, ϕ is the level-set function defined as a signed distance function regarding to Γ , the burning rate \dot{r}_b represents the normal regression velocity caused by surface pyrolysis, gasification or sublimation [10, 11].

The connecting conditions across the gas-solid interface are formulated as

$$[T] = 0, \quad (8)$$

$$[\vec{U} \times \vec{n}] = 0, \quad (9)$$

$$[\rho(\vec{U} \cdot \vec{n} + \dot{r}_b)] = 0, \quad (10)$$

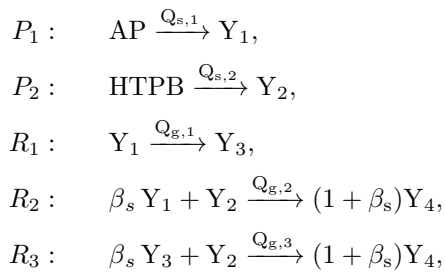
$$[\vec{q} \cdot \vec{n}] = \dot{m} q_L, \quad (11)$$

$$[\vec{j}_k \cdot \vec{n}] = -\dot{m} [Y_k], \quad (12)$$

60 where $[\cdot] = (\cdot)_g - (\cdot)_s$ denotes the jump from Ω_g to Ω_s , \vec{n} is the surface unit normal pointing into Ω_g , $\vec{j}_k =$
 61 $-\lambda_g/c_p \nabla Y_k$ is the diffusive flux vector of the k -th species and $\vec{q} = -\lambda \nabla T$ is the heat flux vector. Note that $\dot{m} = \rho_s \dot{r}_b$
 62 is the mass flux and the latent heat q_L is assigned as constant in Eq. (11).

63 *2.2. Chemical modeling*

A simplified global reaction mechanism [11, 12] is adopted, which consists of 5 global reactions and 6 symbolic species. Specifically,



64 where P_1 and P_2 model the surface behaviors (e.g. decomposition, sublimation, gasification or pyrolysis) of AP and
 65 HTPB, respectively, with the corresponding latent heats $Q_{s,1}$ and $Q_{s,2}$ (positive if exothermic) due to phase change,
 66 other remaining reactions R_i with the heat release rate $Q_{g,i}$ ($i = 1, 2, 3$) describe the evolution of flames [13], β_s is
 67 the overall mass-based AP/HTPB stoichiometric ratio [7, 12]. Molecular weights of gaseous symbolic species (Y_1 ,
 68 Y_2 , Y_3 , and Y_4) are assumed to be identical.

69 The instantaneous burning rate \dot{r}_b of each component is primarily determined by the interface temperature (T_w) [7,
 70 14]. The relation can be formulated as the following Arrhenius law

$$\dot{r}_b = A \exp \left\{ - \frac{E/R}{T_w} \right\}, \quad (13)$$

71 where both the pre-exponential term A and the activation energy E are empirically determined constants. The reaction
 72 rate $\dot{\omega}_i$ for R_i ($i = 1, 2, 3$) is expressed in a unified form as

$$\dot{\omega}_i = D_i p^{n_i} [\text{Y}_1]^{e_{1,i}} [\text{Y}_2]^{e_{2,i}} [\text{Y}_3]^{e_{3,i}} \exp \left\{ - \frac{E_i/R}{T_g} \right\}, \quad (14)$$

73 where D_i is the pre-exponential constant, n_i is the pressure exponent, $[\text{Y}_k]$ denotes the mass fraction of the k -th
 74 species, and E_i is the activation energy.

75 All the kinetic parameters are identical to that in Ref. [12]. By presuming constant adiabatic flame temperature
 76 of pure AP ($T_{\text{ad}}^{\text{AP}}$) and the stoichiometric mixture ($T_{\text{ad}}^{\text{mix}}$), heat release from each reaction can be determined from
 77 energy relations [15, 7, 12, 6]. Details of all physical properties and kinetic parameters are included in Table. 1 for
 78 completeness.

Quantity	Value	Unit
$\lambda_{AP}, \lambda_{HTPB}$	0.405, 0.276	$W m^{-1} K^{-1}$
c_p, c_{AP}, c_{HTPB}	0.3, 0.3, 0.3	$kcal kg^{-1} K^{-1}$
ρ_{AP}, ρ_{HTPB}	1950, 920	$kg m^{-3}$
MW	26	$kg kmol^{-1}$
A_{AP}, A_{HTPB}	$1.45 \times 10^5, 1.036 \times 10^3$	$cm s^{-1}$
$E_{AP}/R, E_{HTPB}/R$	11000, 7500	K
D_1, D_2, D_3	$4.11 \times 10^1, 2.35 \times 10^4, 9.5 \times 10^1$	$g cm^{-3} s^{-1} bar^{-n}$
n_1, n_2, n_3	2.06, 2.06, 1.60	
$e_{1,1}, e_{2,1}, e_{3,1}$	1, 0, 0	
$e_{1,2}, e_{2,2}, e_{3,2}$	3.3, 0.4, 0	
$e_{1,3}, e_{2,3}, e_{3,3}$	0, 1, 1	
$E_1/R, E_2/R, E_3/R$	3000, 8500, 8500	K
$Q_{s,1}, Q_{s,2}$	-80, -66	$kcal kg^{-1}$
$Q_{g,1}, Q_{g,2}, Q_{g,3}$	410, 7403, 4396	$kcal kg^{-1}$

Table 1: Physical properties and kinetic parameters utilized in the mesoscale combustion model

79 3. Computational methodology

80 A partitioned strategy has been developed to solve such a multi-physics problem [9, 8]. As illustrated in Fig. 2, the
 81 solution in each phase is separated from each other by employing two sets of overlapped meshes. The unstructured
 82 mesh is adopted in the solid phase to accommodate the heterogeneous structure of the composite (with AP crystals and
 83 the HTPB binder), where the solid conduction Eq. (6) is solved. The randomly distributed AP crystals are generated
 84 by the Monte-Carlo method [16] with packing examples presented in Sec. 4. The Cartesian grid is employed for
 85 gas-phase computation to ensure numerical robustness. In addition, from the sake of flexibility, interface tracking by
 86 level-set is also implemented on the unstructured mesh. Solutions on these two meshes will be coupled through the
 87 interface conditions.

88 The level-set equation is discretized by the finite-element method (FEM) [17] and Eq. (7) is time-marched in an
 89 explicit manner. The resulted contour of $\phi = 0$ is explicitly interpolated to describe the evolution of Γ . At each
 90 time-step, the solid-phase mesh is intersected by Γ . As depicted in Fig. 3, below Γ is the *active* solid phase, where
 91 the conduction Eq. (6) is solved via the finite-volume method (FVM). It is worth noting that although the gas-solid
 92 interface moves, the solid-phase mesh is fixed throughout the simulation to avoid the undesirable interpolation error.

93 The thermal coupling conditions Eq. (8) and (11) are numerically realized by a non-iterative solution procedure [9].
 94 As depicted in Fig. 4, the gradient operator in Eq. (11) is discretized by the Green-Gauss theorem on each side of the

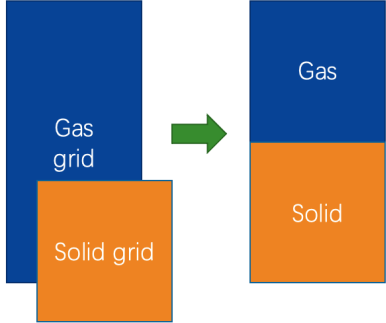


Figure 2: The solid grid (unstructured) and gas grid (Cartesian) are first generated separately. Solutions on these two grids will then be coupled via the interface conditions.

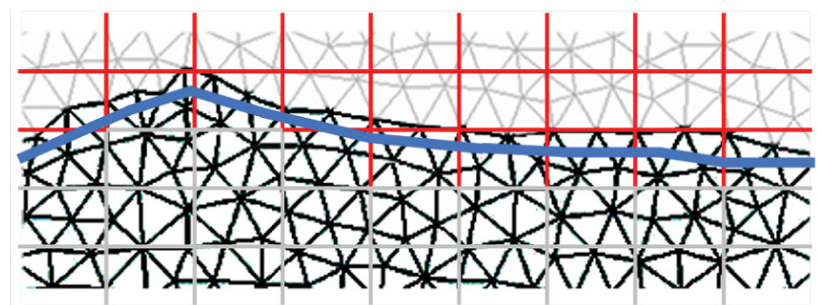


Figure 3: Grid layout around the gas-solid interface (Γ) in a two-dimensional view [9]. The Ω_g (red quadrilaterals) and Ω_s (black triangles) meshes overlap. The gas-solid interface Γ (blue line in the middle) is identified by performing the level-set algorithm on the solid-phase mesh. Cells in grey, i.e. these above Γ in Ω_s and below Γ in Ω_g , will not participate in computation.

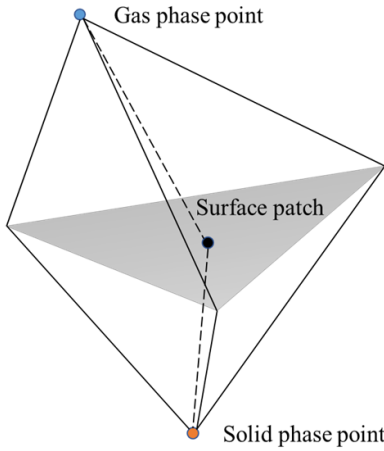


Figure 4: Control volume constructed on both sides of each gas-solid interface element for solving the interface temperature [9, 8].

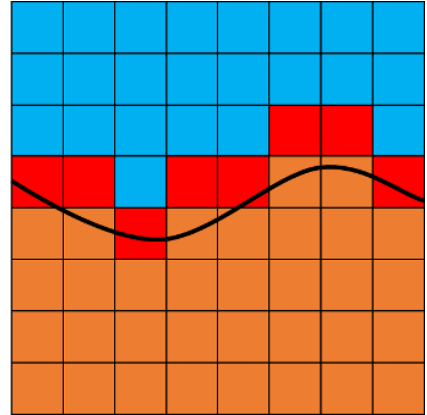


Figure 5: Classification of Cartesian grid cells near the gas-solid interface [8]. Blue cells are those in the gas phase unaffected by IBM; Brown cells underneath the solid phase do not participate in any calculation; Red cells denote the IBM source boundary (red) region, where source terms are imposed.

95 constructed control volume, from which a linear system can be formulated to solve the interface temperature field
 96 (T_w) at each time step. Eq. (9) implies that the escaped mass is injected into Ω_g solely along the surface normal
 97 direction. In the immersed-boundary method, as shown in Fig. 5, conditions for mass flux Eq. (10) and species flux
 98 Eq. (12) are converted into source terms [8] and then distributed to the source boundary cells during the gas-phase
 99 calculation.

100 For the low Mach number reacting flow simulation, Eq. (1)-(4) are consequently solved by a semi-implicit
 101 pressure-based solver [18], in which the projection method is adopted to handle the pressure-velocity-density cou-
 102 pling. The governing equations are discretized by FVM spatially and temporally marched by the three-stage Runge-
 103 Kutta scheme. The convective and diffusive terms adopt the upwind scheme limited by the MLP limiter [19] and the

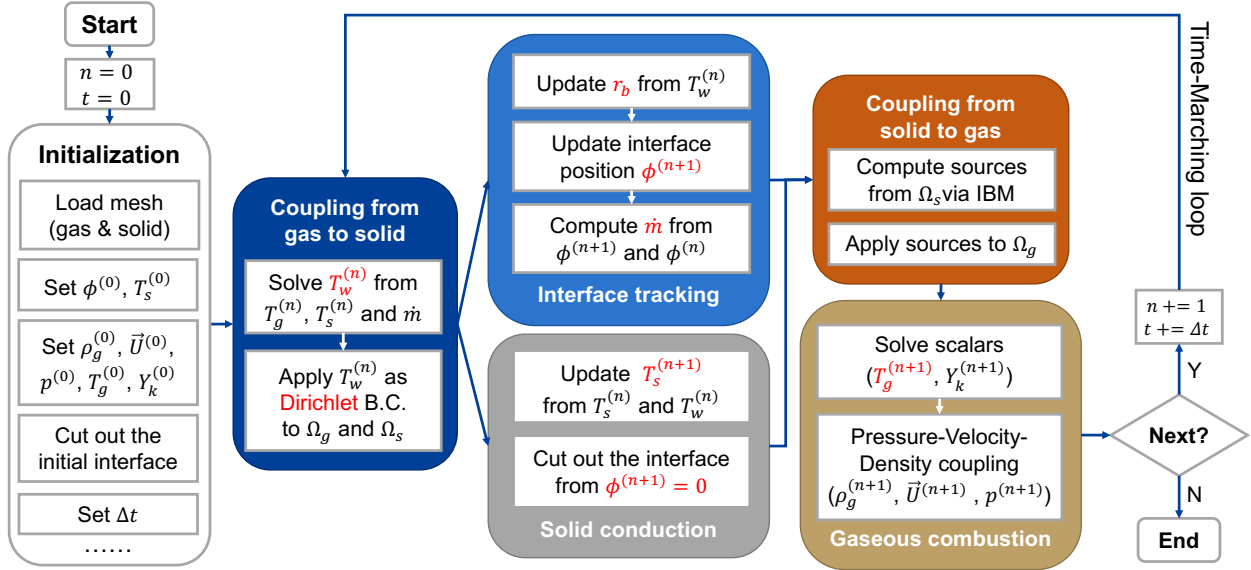


Figure 6: Overall solution procedure for simulating mesoscale AP/HTPB composite propellant combustion.

104 central scheme, respectively. The overall solution procedure of the proposed numerical framework is illustrated in
105 Fig. 6.

106 4. Results and Analyses

107 Two Miller packs [20] are tested in this study: SD-III-88-21 (denoted as M21), and SD-III-88-24 (denoted as
108 M24). Geometrically, the AP crystals are assumed to be spherical. For both the M21 and the M24 pack, the packing
109 fraction of AP is 76.6% (by volume), leading to $\beta_s = 6.938$ in reaction R_2 and R_3 . The remaining space is filled with
110 HTPB. Details of the generated digital packs are listed in Table. 2. For numerical feasibility, undersized AP spheres
111 (i.e., less than 50 μm in the M21 pack, less than 20 μm in the M24 pack) need to be homogenized into the binder
112 background [21]. Thus, bi-modal packs are constructed, as shown in Fig. 7a and Fig. 7c.

113 The burning rate is of particular importance for the engineering design purpose. The calculated burning rates under
114 different pressures are recorded in Fig. 7b and Fig. 7d, together with the results produced by the Rocfire code [22] for
115 comparison. Despite a maximum deviation about 38% (M24 pack at 4.83 MPa), overall the present simulation results
116 match well the experimental measurements.

117 A typical instantaneous flow field is presented in Fig. 8a. As aforementioned, the heterogeneous composite leads
118 to variable local burning rates and thus the corrugated gas-solid interface, which will also influence the distribution of
119 interface temperature. Similarly, streamlines assume curved close to the interface, but tend to be straight downstream
120 in most part of the gas phase Ω_g . Fig. 8b shows the interface temperature with the velocity vectors projected onto $x-y$
121 plane. Typically the parts covered with AP particles (in circles) are relatively cold. Evolution of the solid phase under
122 different pressures are depicted in Fig. 9, from which the uneven deformation of the gas-solid interface due to the

		M21	M24
Composition of AP crystal (by mass)	400 μm	31.6%	-
	200 μm	31.6%	31.6%
	50 μm	10.5%	42.1%
	20 μm	13.7%	13.7%
	Total	87.4%	87.4%
Number of AP crystal (resolved)	400 μm	14	-
	200 μm	114	8
	50 μm	-	672
	20 μm	-	-
	Total	128	680
Size		$(1200 \mu\text{m})^3$	$(500 \mu\text{m})^3$
Number of tetrahedrons (for solid phase)		$\approx 150,000$	$\approx 100,000$
Number of hexahedrons (for gas phase)		$50 \times 50 \times 100$	$32 \times 32 \times 64$

Table 2: Packing and meshing information of the digitally generated AP/HTPB composite propellant at the mesoscale.

123 structure heterogeneity can be clearly recognized. With the increase of pressure, the surface temperature on average
 124 elevates and the surface becomes more corrugated, in consistency with the burning rate results in Fig. 7. More careful
 125 observation indicates that on the surface the AP and HTPB parts can locally protrude or recesses differently, depending
 126 on the operation conditions [23], e.g. the AP/HTPB mass ratio and the system pressure. In Fig. 9, especially for the
 127 higher pressure (20.7 MPa) case, the AP particle parts are prone to be concave.

128 *4.1. Definition of the flame front*

129 Because of the (large) distortion of the solid-gas interface, quantification of the flame front for the solid combustion
 130 case is not straightforward. Locating the flame close to the interface is inspired from the projected components of
 131 velocity on the horizontal $x - y$ plane, defined as

$$\vec{U}_\perp = (\bar{\bar{I}} - \vec{k}\vec{k}) \cdot \vec{U}, \quad (15)$$

132 where $\bar{\bar{I}}$ is the identity tensor and the vector $\vec{k} = (0, 0, 1)^T$ approximates the averaged direction of the flow velocity
 133 downstream. In simple, \vec{U}_\perp represents the velocity induced by the distorted gas-solid interface. An visual example of
 134 this projected velocity is shown in Fig. 8b. Typically, regions with large \vec{U}_\perp magnitude accompany sharp change of
 135 the temperature. If the domain is large enough, \vec{U}_\perp would, in principle, have no preferential orientation. Therefore, it

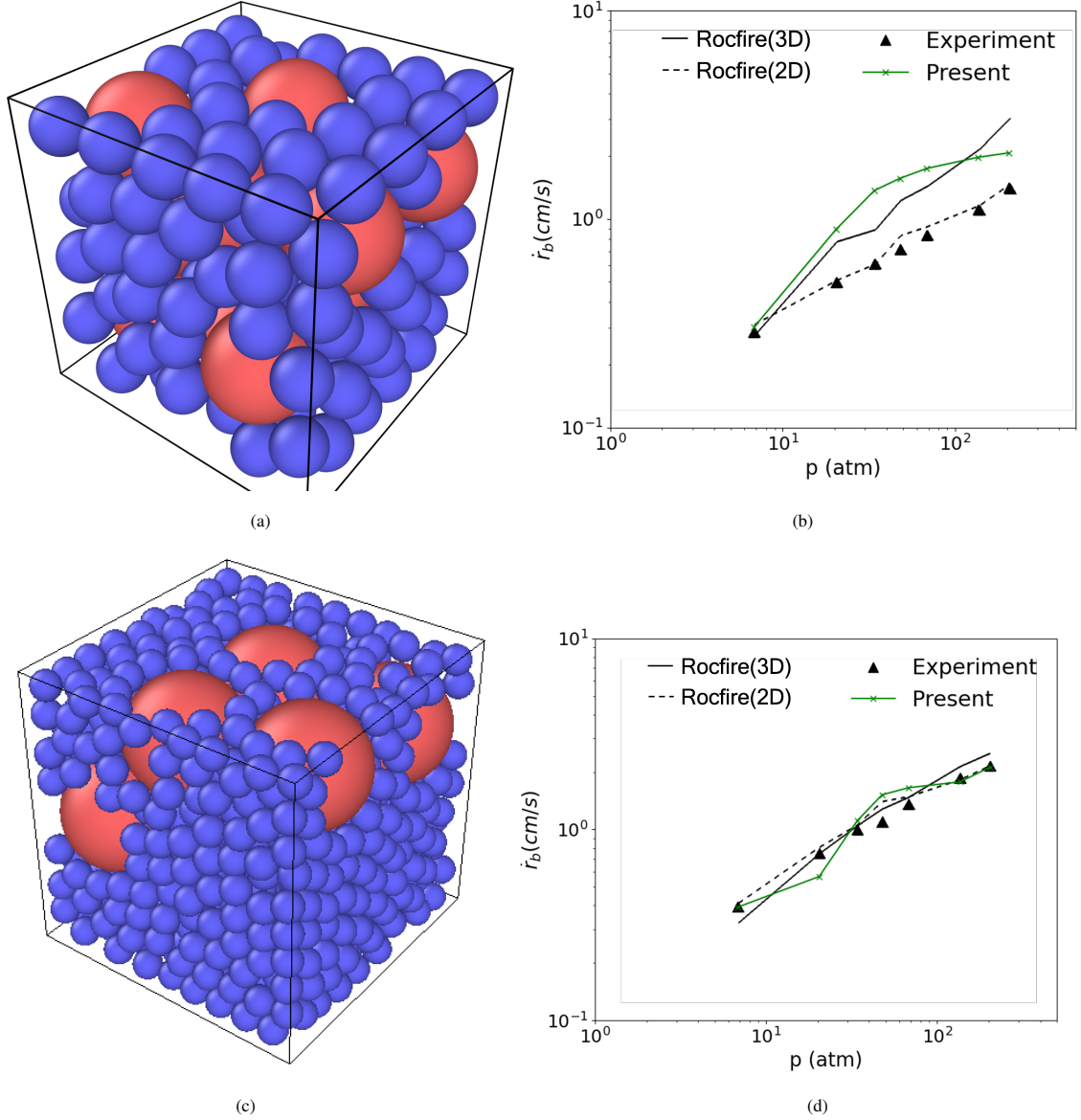


Figure 7: Verification of the proposed numerical framework by predicting the burning rates of two Miller packs over a wide range of pressure conditions. (a) and (c) are bi-modal geometry modeling the heterogeneity of the AP/HTPB composite propellants for the M21 pack and the M24 pack, respectively, in which red and blue spheres represent large and small AP crystals, respectively. (b) and (d) are the simulated burning rates for the M21 pack and the M24 pack, respectively, together with the Rocfire results [22] for comparison.

is meaningful to consider the root mean square (r.m.s.) of \vec{U}_\perp , i.e.

$$U_{\perp}^{\text{r.m.s.}}(t, \bar{z}) = \sqrt{\frac{1}{S} \iint_S ||\vec{U}_\perp(t, x, y, z)||^2 dx dy}, \quad (16)$$

where S is the area of the horizontally-sliced plane, $\bar{z} = \frac{z}{h}$ is the normalized vertical position with h being the grid spacing.

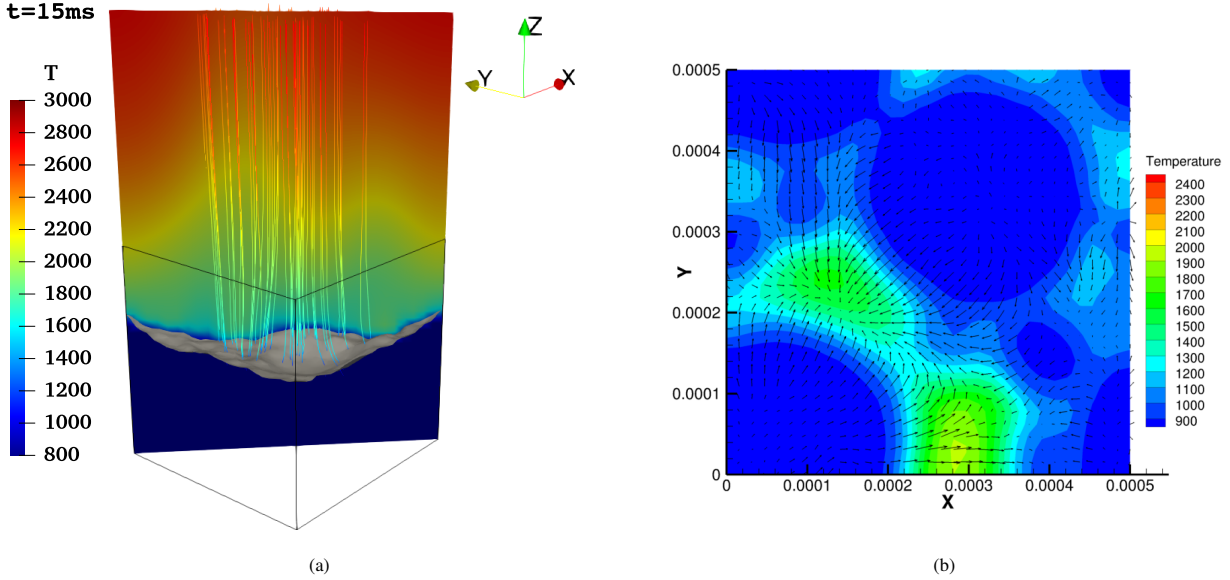


Figure 8: Instantaneous flow field of the M24 pack: (a) a cross cut under 3.45 MPa at $t = 15$ ms, in which the streamlines are curved close to the gas-solid interface (gray) and tend to be straight downstream, while the background color indicates the temperature distribution; (b) interface temperature with the projected velocity \vec{U}_\perp on a horizontally sliced plane. Regions with large \vec{U}_\perp magnitude typically accompany sharp change of the temperature. Units of spatial coordinate and temperature are m and K, respectively.

139 Figure 10 presents the evolution of $U_{\perp}^{\text{r.m.s.}}$ at two typical pressures of the M24 pack. $U_{\perp}^{\text{r.m.s.}}$ vanishes inside the
 140 solid phase and peaks abruptly near the gas-solid interface. Above the peak position, $U_{\perp}^{\text{r.m.s.}}$ decays smoothly. Such
 141 profiles are consistent with the instantaneous flow visualization in Fig. 8a, where the streamlines near the interface are
 142 curved and then gradually become straight. Moreover, by comparing the evolution of $U_{\perp}^{\text{r.m.s.}}$ at distinct instants, the
 143 peak value of $U_{\perp}^{\text{r.m.s.}}$ increases with time after initial ignition, varies after the establishment of combustion and then
 144 decreases toward the end of combustion.

145 Physically, shifting from the gas-solid interface to the flame zone, the temperature, the projected velocity and
 146 $U_{\perp}^{\text{r.m.s.}}$ increase, while after the flame zone, gas expansion will redirect the velocity along the upward direction to
 147 reduce the $U_{\perp}^{\text{r.m.s.}}$. Therefore, the peak position of $U_{\perp}^{\text{r.m.s.}}$ can be defined as the location of the gaseous flame front for
 148 the heterogeneous solid combustion case. Although the flame zone is conventionally considered as the intense reaction
 149 rate or heat release zone, the $U_{\perp}^{\text{r.m.s.}}$ peak characterization provides an alternative guidance for analyses, especially for
 150 experimental diagnoses.

151 To better justify this new definition, the spatial correlation between reaction rates and $U_{\perp}^{\text{r.m.s.}}$ are investigated. At
 152 each time t , the averaged reaction rates $\bar{\omega}_i$ on each normalized vertical position \bar{z} are calculated as

$$\bar{\omega}_i(t, \bar{z}) = \frac{1}{S} \iint_S \dot{\omega}_i(t, x, y, z) dx dy, \quad (i = 1, 2, 3), \quad (17)$$

153 where S is the area of the horizontally-sliced plane. The normalized vertical position \bar{z}_i^* , where the maximum value

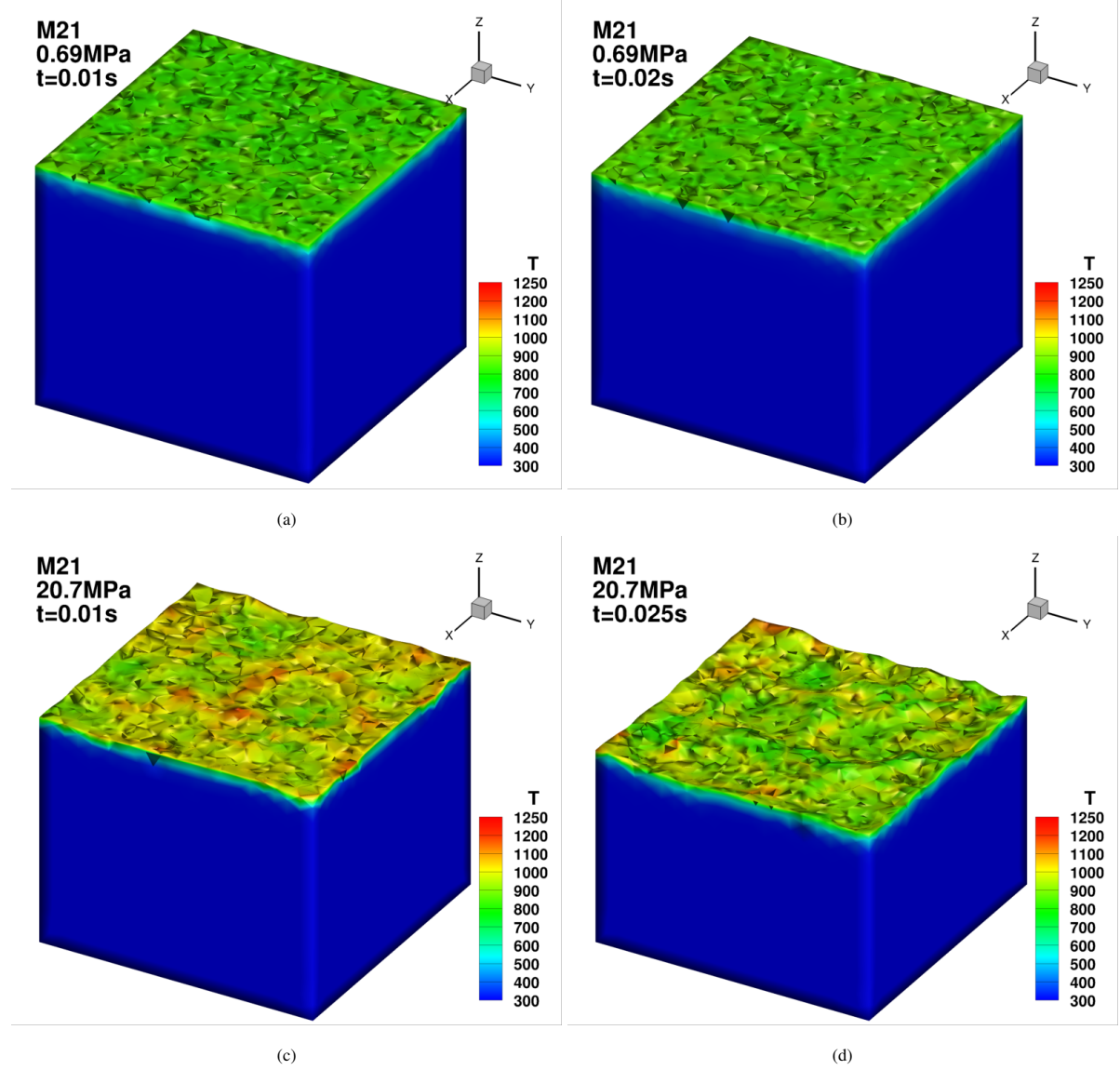


Figure 9: Solid-phase evolution history of the M21 pack. (a) under 0.69 MPa at $t = 10$ ms; (b) under 0.69 MPa at $t = 20$ ms; (c) under 20.7 MPa at $t = 10$ ms; (d) under 20.7 MPa at $t = 25$ ms. At elevated pressure AP crystals escape faster than binder, leading to interface dimples.

154 of $\bar{\omega}_i(t, \bar{z})$ occur, are recorded at each time step. Namely,

$$\bar{\omega}_i(t, \bar{z}_i^*) = \max \{ \bar{\omega}_i(t, \bar{z}) | 0 \leq \bar{z} \leq N_z \}, \quad (i = 1, 2, 3), \quad (18)$$

155 where N_z is the number of grid cells in vertical direction. Similarly, the normalized vertical position $\bar{z}_{U_\perp}^*$ is defined
156 for $U_\perp^{\text{r.m.s.}}$ as

$$U_\perp^{\text{r.m.s.}}(t, \bar{z}_{U_\perp}^*) = \max \{ U_\perp^{\text{r.m.s.}}(t, \bar{z}) | 0 \leq \bar{z} \leq N_z \}. \quad (19)$$

157 As shown in Fig. 11, under typical pressure conditions the recorded \bar{z}_i^* ($i = 1, 2, 3$) and $\bar{z}_{U_\perp}^*$ for both M21 and M24

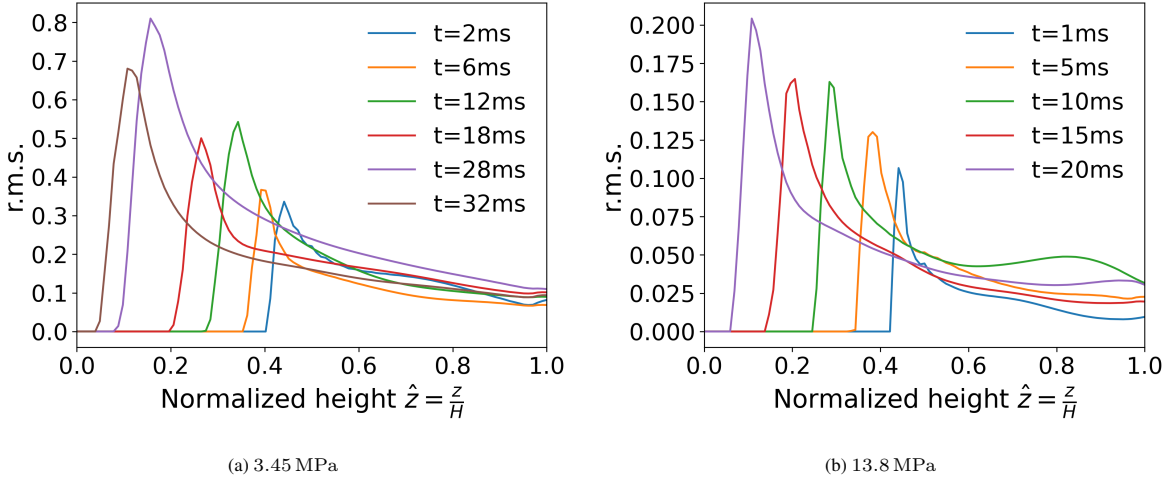


Figure 10: Evolution of $U_{\perp}^{\text{r.m.s.}}$ on typical pressure conditions for the M24 pack. \hat{z} is normalized by the height of the entire domain.

158 packs are well correlated.

159 Further comparison between Fig. 10a and Fig. 10b reveals the dependence of the peak $U_{\perp}^{\text{r.m.s.}}$ on the background
160 pressure p . At a given position $\hat{z} = 0.2$ for example, relation between p and the peak $U_{\perp}^{\text{r.m.s.}}$ peak is presented in
161 Fig. 12. Higher pressure leads to twofold influences on $U_{\perp}^{\text{r.m.s.}}$. On the one hand, higher pressure and thus more
162 strongly varying local burning rates make the gas-solid interface more corrugated, which will enlarge $U_{\perp}^{\text{r.m.s.}}$. On the
163 other hand, the elevated pressure will increase the gas density ρ_g and thus decrease the flow velocity to reduce $U_{\perp}^{\text{r.m.s.}}$.
164 The observation that $U_{\perp}^{\text{r.m.s.}}$ peak decreases with p in Fig. 12 indicates that the second effect is more dominate and the
165 velocity fluctuation is overall *suppressed* by pressure increase.

166 4.2. Conditional statistics based on Lagrangian tracing

167 Influence of composite heterogeneity can also be explored from the Lagrangian tracing analyses. After combustion
168 is stably established, the evolution of fluid parcels originated from different composites, either AP or binder, are shown
169 in Fig. 13 and Fig. 14.

170 For the AP-released and binder-released fluid parcels, the evolution of temperature and reactants (Y_1 , Y_2 and Y_3)
171 undergoes quite different paths. Temperature in Fig. 13a has a longer increasing process, while it reaches maximum
172 rapidly and then levels off in Fig. 14a. Such a difference is primarily caused by a much higher concentration of Y_2
173 and thus more intensive reaction in Fig. 14c. This scenario can be evidenced by the reaction rates $\dot{\omega}_2$ (for reaction R_2)
174 and $\dot{\omega}_3$ (for reaction R_3) in Fig. 14b and Fig. 13b. It can be seen that $\dot{\omega}_{2,3}$ conditional on binder-released fluid parcels
175 are substantially larger (almost 10 times) than the binder-released fluid parcels' results. In particular, $\dot{\omega}_3$ in Fig. 13b
176 lags behind $\dot{\omega}_1$ and $\dot{\omega}_2$, as the binder pyrolyzed species Y_2 needs to be advected after $\dot{\omega}_1$ and $\dot{\omega}_2$ and then reacts, which
177 is different from the Fig. 14b case.

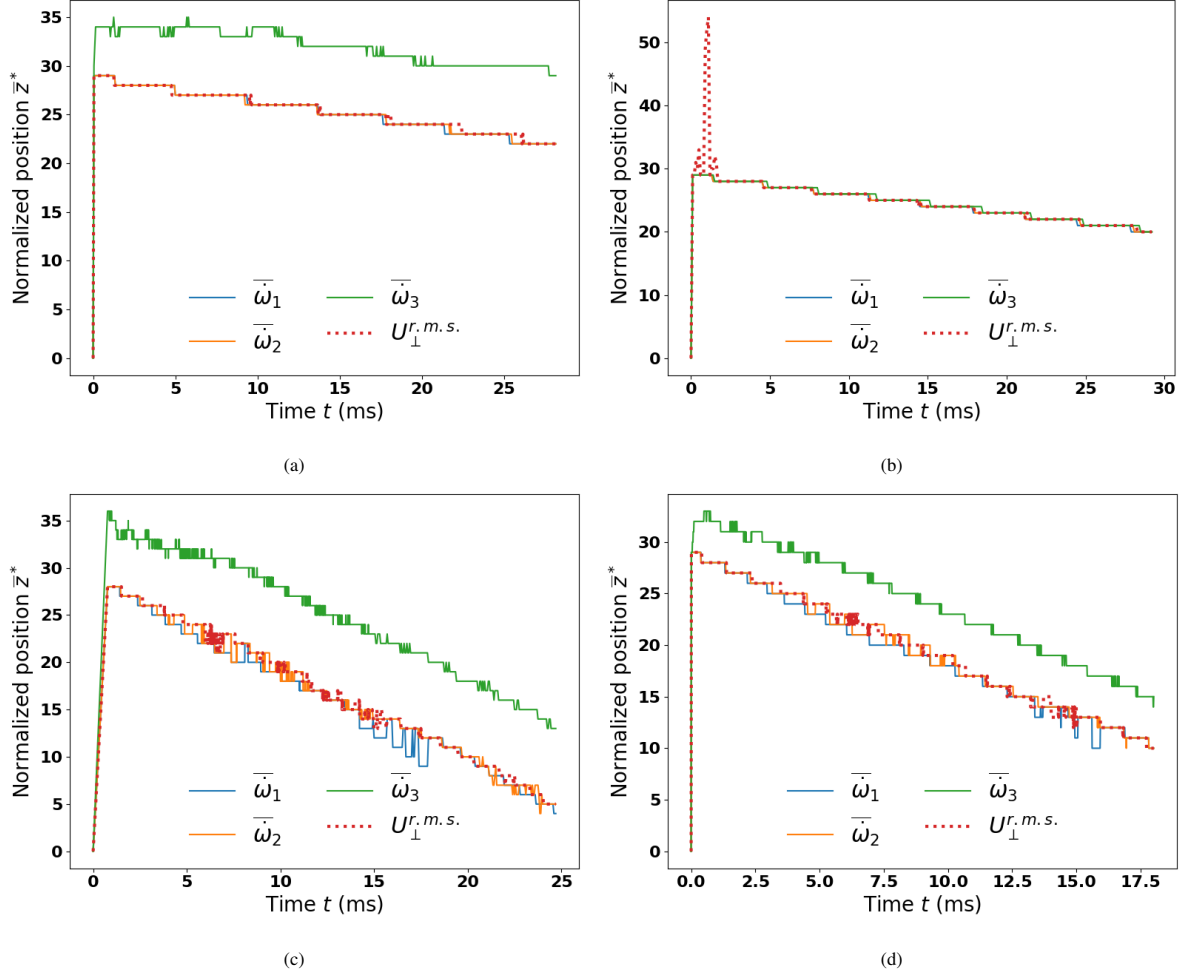


Figure 11: Locations of the maximum gas-phase averaged reaction rate $\bar{\omega}_i$ ($i = 1, 2, 3$) and $U_{\perp}^{r.m.s.}$: (a) M21 pack under 2.07 MPa; (b) M21 pack under 20.7 MPa; (c) M24 pack under 4.83 MPa; (d) M24 pack under 6.89 MPa.

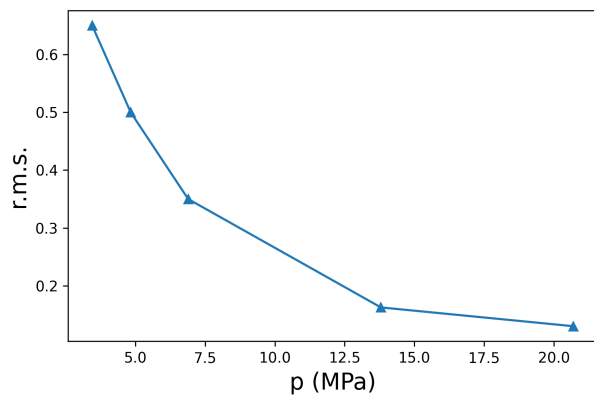
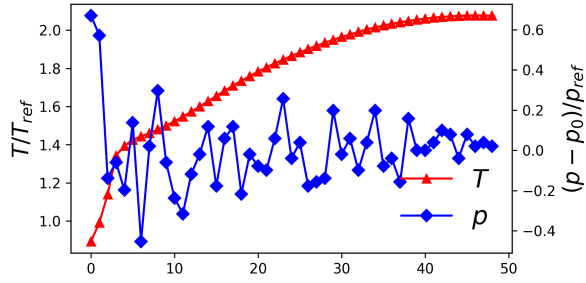
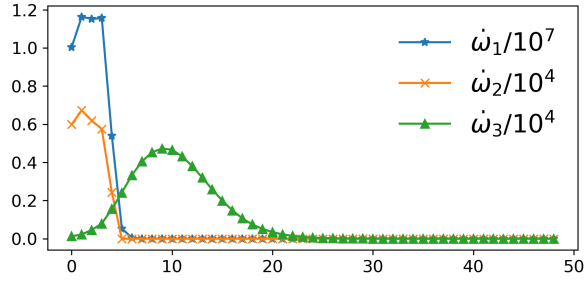


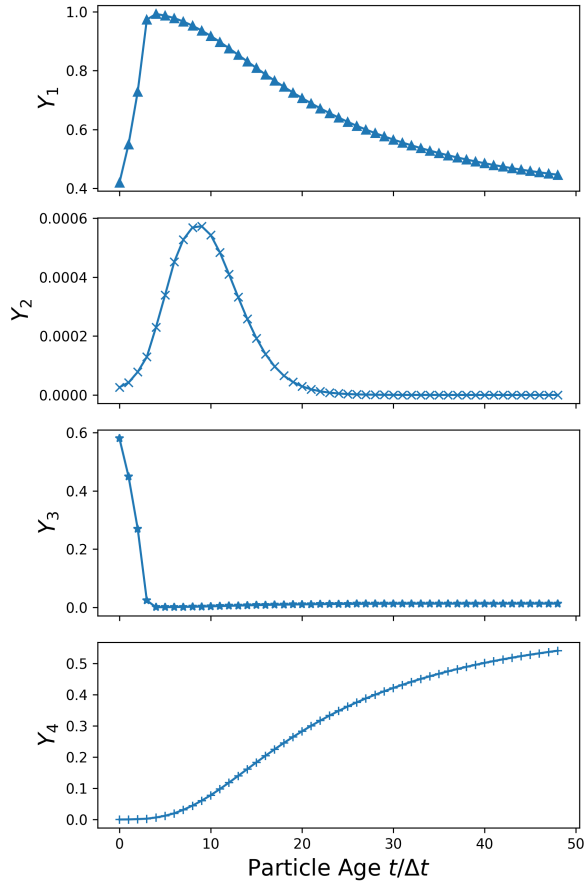
Figure 12: Dependence of $U_{\perp}^{r.m.s.}$ with the background pressure at $\hat{z} = 0.2$ for the M24 pack.



(a)

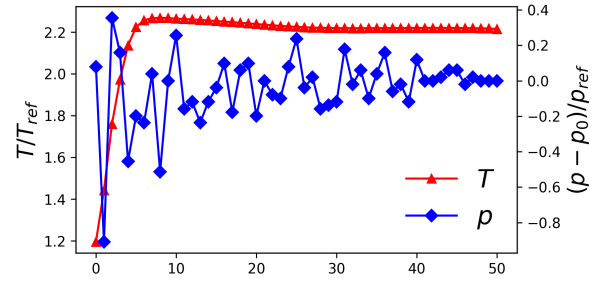


(b)

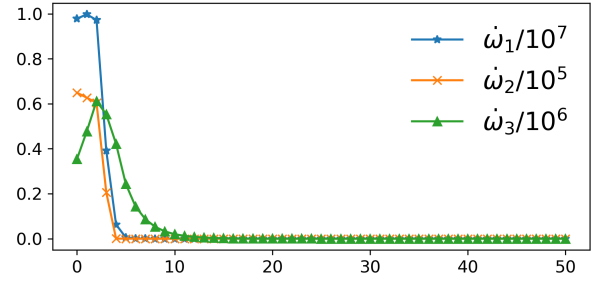


(c)

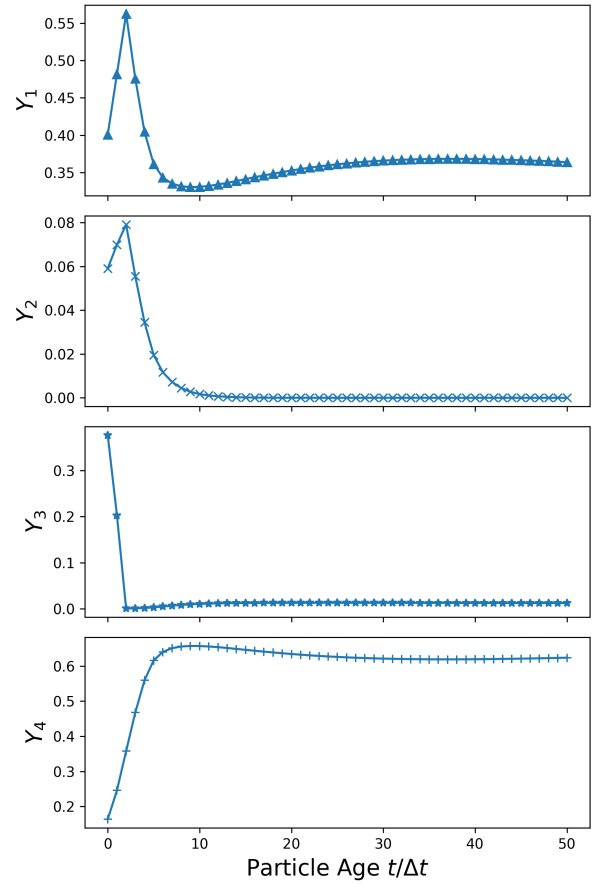
Figure 13: Evolution on the tracer released from an **AP** crystal within the M24 pack under 20.7 MPa ($\Delta t = 10 \mu\text{s}$, $T_{\text{ref}} = 1400 \text{ K}$, $p_0 = 20.7 \text{ MPa}$, $p_{\text{ref}} = 0.001 \text{ atm}$): (a) Primitive variable; (b) Reaction rate; (c) Species concentration.



(a)



(b)



(c)

Figure 14: Evolution on the tracer released from **HTPB** within the M24 pack under 20.7 MPa ($\Delta t = 10 \mu\text{s}$, $T_{\text{ref}} = 1400 \text{ K}$, $p_0 = 20.7 \text{ MPa}$, $p_{\text{ref}} = 0.001 \text{ atm}$): (a) Primitive variable; (b) Reaction rate; (c) Species concentration.

178 **5. Conclusions**

179 In summary, a new numerical framework has been introduced for composite propellant combustion simulation at
180 the mesoscale. The structured and unstructured meshes are adopted for the gas phase and solid phase, respectively. The
181 level-set approach is used on the unstructured mesh to identify solid-gas interface with complex geometry. Information
182 exchange between these two overlapping meshes is realized with the immersed-boundary method to ensure physical
183 conservation relations, such as the mass, species and energy balance across the gas-solid interface. Besides, the
184 thermal connecting conditions are fully embodied by solving the temperature field on the gas-solid interface in a
185 efficient and non-iterative manner.

186 Simulation results for the typical Miller pack justifies the applicability of this framework. Visualization of the
187 gas-phase flow field shows that the streamlines are curved close near the regressing gas-solid interface and then tend
188 to be straight downstream. The peak of the projected velocity fluctuation, i.e. $U_{\perp}^{\text{r.m.s.}}$, provides an alternative
189 characterization of the flame zone near the regressing interface. The $U_{\perp}^{\text{r.m.s.}}$ peak value decreases with the pressure is
190 under the joint control of the gas-solid interface structure and the flow velocity. Moreover, conditional statistics of
191 the evolution processes of fluid parcels released from either AP or binder are comparatively studied, showing distinct
192 chemical kinetics of AP-rich and binder-rich reactions. Further investigation on multi-modal packs under broader
193 operation conditions will help to gain deeper insights of the composite propellant combustion physics.

194 **References**

- 195 [1] Y. Fabignon, J. Anthoine, D. Davidenko, R. Devillers, J. Dupays, D. Gueyffier, J. Hijlkema, N. Lupoglazoff, J.-M. Lamet, L. Tesse, A. Guy,
196 C. Erades, Recent advances in research on solid rocket propulsion, *Aerospace Lab J.* 11 (2016) 1–15.
- 197 [2] T. Gaduparthi, M. Pandey, S. R. Chakravarthy, Gas phase flame structure of solid propellant sandwiches with different reaction mechanisms,
198 *Combust. Flame* 164 (2016) 10–21.
- 199 [3] S. Isert, S. F. Son, The relationship between flame structure and burning rate for ammonium perchlorate composite propellants, in: M. K.
200 Shukla, V. M. Boddu, J. A. Steevens, R. Damavarapu, J. Leszczynski (Eds.), *Energetic Materials: From Cradle to Grave*, Springer International
201 Publishing, Cham, 2017, pp. 171–211.
- 202 [4] T. L. Jackson, Modeling of heterogeneous propellant combustion: A survey, *AIAA J.* 50 (2012) 993–1006.
- 203 [5] S. Gallier, M. Plaud, A model for solid propellant burning fluctuations using mesoscale simulations, *Acta Astronaut.* 158 (2019) 296–303.
- 204 [6] J. Buckmaster, T. Jackson, M. Ulrich, Numerical modeling of heterogeneous propellant combustion, 37th Joint Propulsion Conference and
205 Exhibit (2001).
- 206 [7] T. L. Jackson, J. Buckmaster, Heterogeneous propellant combustion, *AIAA J.* 40 (2002) 1122–1130.
- 207 [8] Y. Zhang, Y. Cang, S. Yang, L. Wang, Heterogeneous propellant combustion with conjugated interface conditions, *Comput. Fluids* 240 (2022)
208 105397.
- 209 [9] Y. Cang, Y. Hu, L. Wang, Y. Shen, Numerical scheme solving the temperature of the interface between gas and heterogeneous solid with
210 phase change, *Int. J. Numer. Meth. Eng.* 123 (2021) 1036–1056.
- 211 [10] X. Wang, T. L. Jackson, L. Massa, Numerical simulation of heterogeneous propellant combustion by a level set method, *Combust. Theory
212 Modell.* 8 (2004) 227–254.
- 213 [11] L. Massa, T. L. Jackson, M. Short, Numerical solution of three-dimensional heterogeneous solid propellants, *Combust. Theory Modell.* 7
214 (2003) 579–602.

- 215 [12] L. Massa, T. L. Jackson, J. Buckmaster, New kinetics for a model of heterogeneous propellant combustion, *J. Propul. Power* 21 (2005)
216 914–924.
- 217 [13] M. W. Beckstead, R. L. Derr, C. F. Price, A model of composite solid-propellant combustion based on multiple flames, *AIAA J.* 8 (1970)
218 2200–2207.
- 219 [14] H. Arisawa, T. B. Brill, Flash pyrolysis of hydroxyl-terminated polybutadiene (HTPB) I: Analysis and implications of the gaseous products,
220 *Combust. Flame* 106 (1996) 131–143.
- 221 [15] A. Hegab, T. L. Jackson, J. Buckmaster, D. S. Stewart, Nonsteady burning of periodic sandwich propellants with complete coupling between
222 the solid and gas phases, *Combust. Flame* 125 (2001) 1055–1070.
- 223 [16] V. Baranau, U. Tallarek, Another resolution of the configurational entropy paradox as applied to hard spheres, *J. Chem. Phys.* 147 (2017)
224 224503.
- 225 [17] Z. Fu, S. Yakovlev, R. M. Kirby, R. T. Whitaker, Fast parallel solver for the levelset equations on unstructured meshes, *Concurr. Comp-Pract.
E* 27 (2015) 1639–1657.
- 226 [18] C. Pierce, Progress-variable approach for large eddy simulation of turbulent combustion, Ph.D. thesis, Stanford University (2001).
- 227 [19] J. S. Park, S.-H. Yoon, C. Kim, Multi-dimensional limiting process for hyperbolic conservation laws on unstructured grids, *J. Comput. Phys.*
228 229 (2010) 788–812.
- 229 [20] R. Miller, Effects of particle size on reduced smoke propellant ballistics, 18th Joint Propulsion Conference (1982).
- 230 [21] M. Chen, J. Buckmaster, T. L. Jackson, L. Massa, Homogenization issues and the combustion of heterogeneous solid propellants, *Proc.
Combust. Inst.* 29 (2002) 2923–2929.
- 231 [22] B. T. Bojko, M. Gross, T. L. Jackson, Investigating dimensional effects on predicting burning rates of heterogeneous solid propellants, *AIAA
Scitech 2019 Forum* (2019).
- 232 [23] M. Gross, T. Hedman, S. Son, T. Jackson, M. Beckstead, Coupling micro and meso-scale combustion models of ap/htpb propellants, *Combust.
Flame* 160 (2013) 982–992.